ACS APPLIED MATERIALS & INTERFACES

Research Article

Cite This: ACS Appl. Mater. Interfaces 2017, 9, 39059-39068

www.acsami.org

Anomalous Corrosion of Bulk Transition Metal Diselenides Leading to Stable Monolayers

Yu-Ting Huang,[†,‡] Akhil Dodda,[§] Daniel S. Schulman,[∥] Amritanand Sebastian,[†,^] Fu Zhang,[∥] Drew Buzzell,[†] Mauricio Terrones,[∥,⊥,△] Shien-Ping Feng,[‡,#] and Saptarshi Das*[,†]

[†]Department of Engineering Science and Mechanics, Pennsylvania State University, University Park, Pennsylvania 16802, United States

[‡]Department of Mechanical Engineering, University of Hong Kong, Pokfulam, Hong Kong

[§]Department of Mechanical Engineering, Amrita Vishwa Vidyapeetham, Amritapuri, Clappana P.O., Kollam, 690525 Kerala, India

[^]Department of Electronics and Communication Engineering, Amrita Vishwa Vidyapeetham, Amritapuri, Clappana P.O., Kollam, 690525 Kerala, India

[∥]Department of Materials Science and Engineering, Pennsylvania State University, University Park, Pennsylvania 16802, United States

[⊥]Department of Physics, Pennsylvania State University, University Park, Pennsylvania 16802, United States

[#]The University of Hong Kong-Zhejiang Institute of Research and Innovation (HKU-ZIRI), Hangzhou, Zhejiang 311300, China

[△]Department of Chemistry, Pennsylvania State University, University Park, Pennsylvania 16802, United States

ABSTRACT: In this paper we provide insight into an anomalous corrosion process, referred to as electroablation (EA), which converts multilayer flakes of transition metal diselenides like $MoSe_2$ into their corresponding monolayers when micromechanically exfoliated on a conductive electrode and subsequently subjected to a high anodic potential inside a conventional electrochemical cell. Photoluminescence intensity maps and scanning transmission electron microscopy (STEM) images confirmed the single crystalline nature and 2H-hexagonal lattice structure of the remnant monolayer $MoSe_2$ flakes, indicating the superior corrosion stability of the monolayers compared to that of the bulk counterpart. It is noted that the EA technique is a low-cost alternative for high-yield synthesis of single crystalline monolayer $MoSe_2$ at room temperature. We also found that the dynamics of such an electro-oxidation-mediated and self-limiting corrosion process differs significantly for $MoSe_2$ and WSe_2. While we were able to engineer the corrosion conditions for the EA process to obtain monolayers of $MoSe_2$, our attempts to obtain monolayers of WSe_2 were largely unsuccessful. Finally, we constructed a phenomenological physical chemistry framework to explain such anomalous corrosion processes in transition metal diselenides.

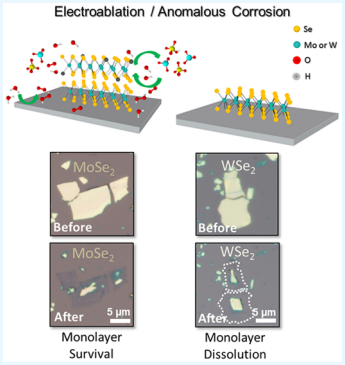

KEYWORDS: *electrochemistry, 2D materials, corrosion, transition metal diselenide, monolayers, electro-oxidation*

INTRODUCTION

The field of two-dimensional (2D) layered materials is rapidly expanding to a larger variety of atomically thin materials ever since the inspirational discovery of graphene. Within this field, the group of transition metal dichalcogenides (TMDs) has attracted great attention owing to their versatile and intriguing physical and chemical properties, particularly at the monolayer limit.[1] The extraordinary van der Waals (vdW) crystal structure of these compounds accounts for the easy cleavage perpendicular to the crystal *c*-axis down to monolayer. Among various TMDs, molybdenum- (Mo-) and tungsten- (W-)based dichalcogenides offer excellent semiconducting properties which make them appealing for electronic applications such as field effect transistors,[2−4] radio frequency transistors,[5,6] low-power transistors,[7] neuromorphic transistors,[8] storage devices,[9,10] and various sensors.[11,12] Moreover, monolayers of MoS_2, WS_2, $MoSe_2$, and WSe_2 exhibit a direct bandgap, which allows their application in solar cells,[13,14] ultrafast photodetectors,[15,16] single-photon emitters,[17,18] light-emitting diodes,[19,20] gain medium for lasers,[21] and various other optoelectronic devices.[22] While early experimental studies used a top-down micromechanical exfoliation technique in order to obtain monolayers of a wide variety of 2D materials,[23−26] it has extremely low yield, and the monolayers are often limited in size. In recent years, significant progress has been made in bottom-up synthesis approaches such as chemical vapor deposition (CVD) which can provide large-area monolayers but requires higher processing temperatures and longer processing times.[27−30] Although the self-limiting electroablation (EA) process does not aim to compete with CVD growth, it is a scientifically intriguing and alternative low-cost synthesis technique for single crystalline monolayer 2D materials with

Received: August 30, 2017
Accepted: October 13, 2017
Published: October 13, 2017

DOI: 10.1021/acsami.7b13107
ACS Appl. Mater. Interfaces 2017, 9, 39059−39068

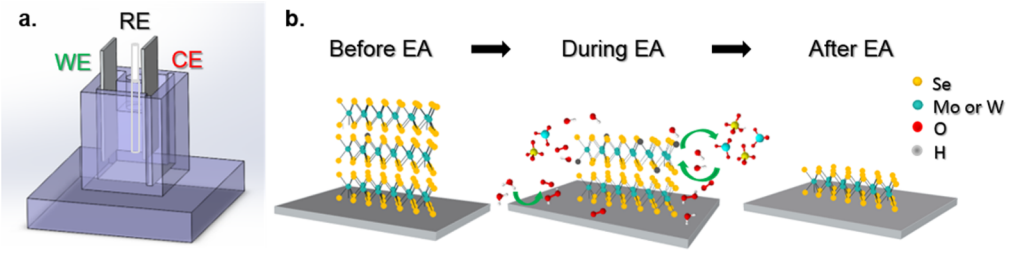

Figure 1. Electroablation (EA) process. (a) Electrochemical cell setup including the working electrode (WE), an Ag/AgCl reference electrode (RE), and a platinum sheet counter electrode (CE). The WE is a conductive TiN/Si substrate with exfoliated flakes. (b) Schematic showing the dynamics of the EA process resulting in monolayer flakes of transition metal disulfides.

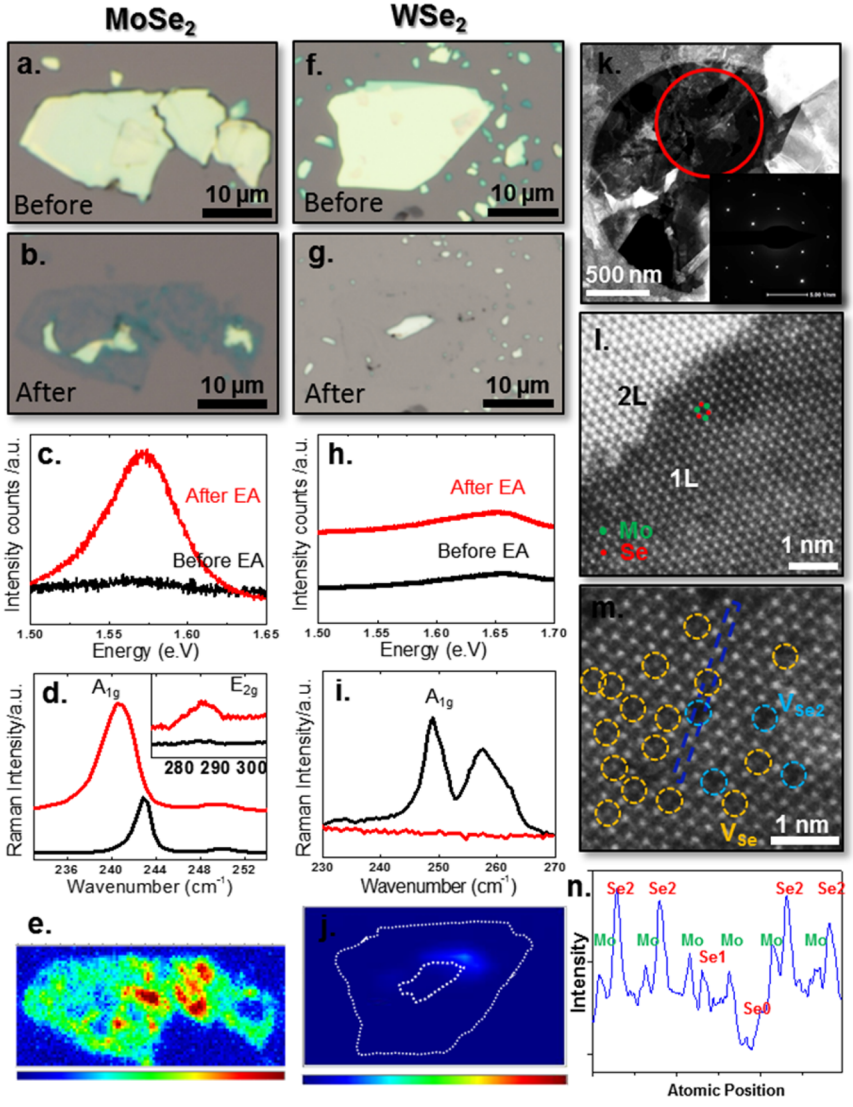

Figure 2. Characterization of electroablated transition metal diselenides. Optical images of a mechanically exfoliated $MoSe_2$ flake (a) before and (b) after 10 s of EA treatment. (c) Photoluminescence (PL) and (d) Raman spectra taken using a 523 nm laser before and after the EA process for $MoSe_2$ near the edges of the flake indicate the monolayer remnant. (e) PL map reinforces the evidence of monolayer $MoSe_2$ after 10 s of EA treatment. Optical images of a WSe_2 flake (f) before and (g) after 10 s of EA treatment. (h) Photoluminescence (PL) and (i) Raman spectra, and (j) PL map for WSe_2 flakes before and after 10 s of EA treatment show complete corrosion of the flake without any monolayer remnant. (k) Low-magnification STEM image of a typical electroablated $MoSe_2$ flake with single-layer and few-layer regions; inset SAED with hexagonal patterns indicates good crystallinity of 2H-phase $MoSe_2$. (l) Atomic resolution annular dark field scanning TEM (ADF-STEM) image of the single-layer $MoSe_2$, Mo (green dots) and Se (red dots) atoms, and sequent layers can be distinguished by the image intensity. (m) ADF-STEM image of the defective single-layer $MoSe_2$ region; (n) the line intensity of the ADF-STEM image identifies the double and single Se vacancies.

DOI: 10.1021/acsami.7b13107
ACS Appl. Mater. Interfaces 2017, 9, 39059−39068

high yield.[31] In fact, the EA process could be complementary to the CVD processes since it can be used to planarize CVD-grown multilayer TMDs into their corresponding monolayers.

We have already demonstrated that the EA technique can be used to convert multilayer MoS_2 and WS_2 flakes,[31] exfoliated on a conductive TiN substrate, into their corresponding monolayers by applying a high anodic potential inside a conventional electrochemical cell as shown in Figure 1a. As described in our earlier article, the basal planes of 2D van der Waals (VdW) materials in general and transition metal disulfides in particular are chemically inert, whereas edge sites are energetically active because of the presence of point defects and/or broken bonds. Therefore, under high anodic potentials, oxidizing species generated in the electrolyte solution progressively corrode/etch/ablate the multilayer MoS_2 and WS_2 flakes from their edges toward the center as shown schematically in Figure 1b. However, such edge reactivity is completely inhibited at the monolayer limit through monolayer/substrate covalent interaction, thus making the monolayers virtually incorrodable. As such, monolayer remnants of MoS_2 and WS_2 are left behind after the ablation of the multilayer flakes making the electroablation (EA) process self-limiting.

In this article, we investigate the feasibility of the EA technique for obtaining monolayers of transition metal diselenides like $MoSe_2$ and WSe_2. $MoSe_2$ is particularly interesting since it finds application in the catalytic hydrogen evolution reaction,[32,33] field effect transistors,[34] and electrochemical intercalation,[35] and it also provides a unique platform to investigate advanced light−matter coupling as it hosts stable and robust excitons with comparably narrow optical resonances.[36,37] Similarly, WSe_2 offers high carrier mobility, and it is one of the rare 2D materials which offers both electron as well as hole transport that is essential for the development of next-generation complementary logic devices.[3,38] As we will elucidate in this article, unlike that for sulfides, the dynamics of the EA process is far more intricate for the selenides and requires rigorous optimization of the pH conditions. Further, we will demonstrate that the EA process differs significantly between $MoSe_2$ and WSe_2 in terms of the final outcome. Although we were successful in obtaining monolayers of $MoSe_2$ by proper experimental conditioning, our attempts to obtain monolayers of WSe_2 were mostly unsuccessful. We were also able to hypothesize the reaction pathways and kinematics of the reactions involved in the EA process for the selenides to explain our experimental findings. It is noted that our ultimate goal is to develop the EA process as a low-cost and high-yield alternative for obtaining monolayers of a wide variety of two-dimensional (2D) layered materials by understanding the fundamental physical and chemical factors that are involved in the process. This article is one step forward to achieving that objective.

EXPERIMENTAL PROCEDURE

The substrates used for this study were Si wafers (resistivity 0.01−0.02 Ω cm) sputtered with 100 nm thick TiN purchased from West Coast Silicon. These substrates were conditioned by heat-treating at 500 °C for 10 min under N_2 ambient using a rapid thermal annealing tool (Allwin21 Heatpulse 610). This annealing step is critical to ensure the chemical stability of our conductive TiN/Si substrates and hence the reproducibility of the electroablation (EA) process. $MoSe_2$ and WSe_2 crystals were purchased from 2D Semiconductors Inc. and were mechanically exfoliated onto the substrates. The mechanical exfoliation provides pristine-quality crystallites of $MoSe_2$ and WSe_2 with an average lateral dimension between 5 and 20 μm and thicknesses ranging from 1 to 100 nm. The electroablation (EA) technique was conducted using a three-electrode electrochemical cell that consisted of the exfoliated substrates as the working electrode (WE), a Ag/AgCl reference (6 mm, BASi) as the reference electrode (RE), and platinum (Pt) sheets as the counter electrode (CE). The electrolyte for the EA technique was prepared with lithium chloride salt ($LiCl_{(s)}$, VWR) in deionized water and with subsequent addition of 37% hydrochloric acid (HCl, EMD Millipore) to achieve acidic solutions of pH = 1−4. The acidity was measured using a calibrated pH meter (Mettler Toledo SevenMulti). The schematic of the electrochemical cell used for EA is provided in Figure 1a.

The electroablation was carried out in the electrochemical cell via a potentiostat (Solartron Analytical 1287). Linear sweep voltammetry and Potentiodynamic (PD) measurements were used to evaluate the electrochemical dynamics of the exfoliated material by scanning from 0 to 2 V (versus Ag/AgCl) at a scan rate of 10 mV/s. The EA was performed at a constant potential to complete the ablation process of multilayer flakes. The electroablation was characterized using Raman spectroscopy to distinguish between multilayers and monolayers, photoluminescence (PL) mapping to confirm the monolayer transformation, and atomic force microscopy (AFM - Bruker Icon) for thickness investigation. The vibrational modes of mono- and multilayer $MoSe_2$ and WSe_2 were characterized using high-resolution Raman spectroscopy and PL (Horiba LabRAM HR spectrometer) with a laser excitation wavelength of 532 nm. The as-prepared $MoSe_2$ was transferred from the TiN substrate to a Quantifoil Au TEM grid by a PMMA-assisted water-transfer method. Transmission electron microscopy, FEI Talos and Titan[3] (60−300) at 80 kV at Pennsylvania State University, was used to examine and study the atomic structure of the $MoSe_2$. The Z-contrast imaging feature of ADF-STEM imaging is used to distinguish the Mo atoms and Se atoms. AFM measurements for thickness evaluation of the electroablation process were made using a Bruker Dimension Icon instrument. Unless otherwise noted, all images were taken after 5 s of EA.

RESULTS AND DISCUSSION

Figure 2a,b shows the optical micrographs of $MoSe_2$ flakes before and after the EA. It is found that the $MoSe_2$ flakes became comparatively transparent after the EA, and the edge area is more transparent than the center area, suggesting the formation of an ultrathin $MoSe_2$ layer. This transformation of multilayer $MoSe_2$ to monolayer can be seen in the photoluminescence (PL) peak intensity map in Figure 2e. The PL map shows an intense signal from the thinner region and yet a much diminished intensity in the bulky region. PL measurements are routinely used in the literature for unambiguous distinction of monolayer TMDs from their multilayer and bulk counterparts.[39] The PL enhancement is a consequence of an indirect to direct bandgap transition that happens only at the monolayer limit. As seen in Figure 2c, the thinner area emits intense PL and exhibits a single prominent maximum at 1.57 eV (792 nm). This emission peak is in excellent agreement with the reported optical bandgap of monolayer $MoSe_2$ (1.57 eV)[40] and thus verifies the formation of monolayer $MoSe_2$ in the EA process. The emission intensity varies across the monolayer area together with a small shift of the luminescence energy. This is related to the Se vacancies already present in the exfoliated material or introduced during the electroablation process.[41] In addition, the Raman spectra in Figure 2d reinforce the evidence of monolayer $MoSe_2$ formation. The Raman active out-of-plane A_{1g} mode is found at 239 cm^{-1} for the monolayer $MoSe_2$.[42] However, the A_{1g} mode shifts toward higher wavenumbers (243 cm^{-1}) in multilayer $MoSe_2$ because of the interlayer interaction along the *c*-axis (A_{1g} mode: the Se atoms in all layers oscillate in phase with respect to the corresponding

DOI: 10.1021/acsami.7b13107
ACS Appl. Mater. Interfaces 2017, 9, 39059−39068

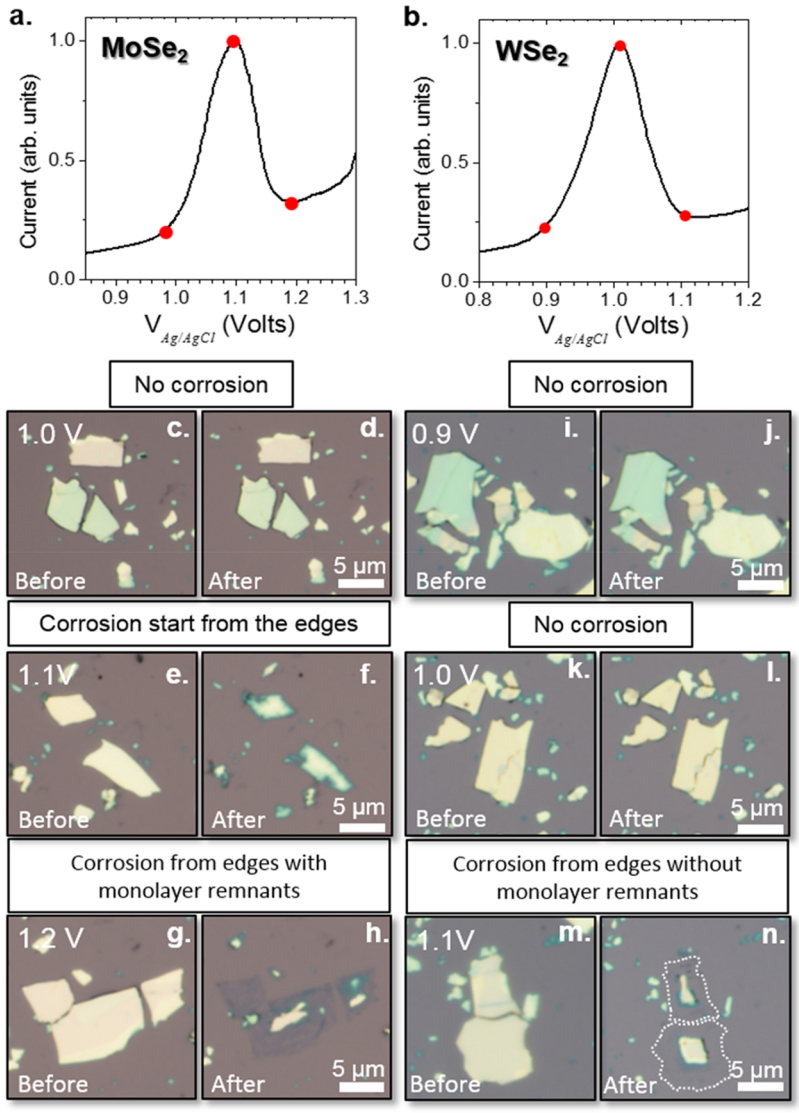

Figure 3. Corrosion and oxidative dissolution of transition metal diselenides. Voltammograms for (a) $MoSe_2$ and (b) WSe_2 from a range 0.8−1.2 V at pH 3 in 1 M LiCl. (c−h) Optical images of $MoSe_2$ flakes prior to and after 5 s of EA treatment at 1.0, 1.1, and 1.2 V. (i−n) Optical images of WSe_2 flakes prior to and after 5 s of EA treatment at 0.9, 1.1, and 1.2 V.

center molybdenum atom). The in-plane E_{2g} mode appears at higher wavenumbers, which is found only in the monolayer at 287.2 cm^{-1} because the vibrational mode is weak in multilayers. Several reports have indicated that, for multilayer $MoSe_2$, the E_{2g} peak is almost invisible at low excitation energies and increases monotonically at excitation energies above 2.54 eV. It was also reported that near the band-to-band transition at ∼2.5 eV, the Raman intensity of the A_{1g} phonon is enhanced, whereas that of the E_{2g} phonon is not.[43,44] It is noted that our Raman study uses a laser excitation wavelength of 532 nm (2.3 eV). As such, the Raman peak E_{2g} is not really visible for bulk $MoSe_2$. The optical images in Figure 2f,g, respectively, present the change of a WSe_2 flake before and after EA treatment. Unlike $MoSe_2$, the WSe_2 multilayer flake was completely corroded away without any monolayer remnant after the EA. Absence of any detectable signal in the PL measurement (Figure 2h), Raman scan (Figure 2i), and PL mapping (Figure 2j) clearly indicates complete corrosion/ablation of the WSe_2 flake. The scanning transmission electron microscopy (STEM) image of the electroablated $MoSe_2$ shown in Figure 2k indicates the monolayer-to-few-layer feature of the flake; the inset corresponding selected area electron diffraction (SAED) pattern reveals the good crystallinity of the as-prepared $MoSe_2$ with a hexagonal structure. The annular dark field scanning TEM (ADF-STEM) image in Figure 2l displays the atomic structure of the monolayer $MoSe_2$ flake, and Mo and Se atoms, and sequent layers can be identified by analyzing the intensity profile due to the Z-contrast (atomic number) characteristics of ADF-STEM imaging. Massive single and double selenium vacancies (V_{Se} and V_{Se_2}) can also be distinguished from the Se_2 column in the perfect lattice (Figure 2m,n).

Figure 3a,b shows the anodic peaks in the linear sweep voltammetry curves for $MoSe_2$ and WSe_2. These voltammetry scans were taken by sweeping the anodic potential from 0 to 2 V versus the Ag/AgCl reference and are at a pH of 3.0. The oxidative dissolution of the multilayer $MoSe_2$ and WSe_2 flakes during the EA process is an irreversible reaction, and thus the anodic peaks can only be seen from the first scan. The optical micrograph pictures in Figure 3c−h and in Figure 3i−n,

DOI: 10.1021/acsami.7b13107
ACS Appl. Mater. Interfaces 2017, 9, 39059−39068

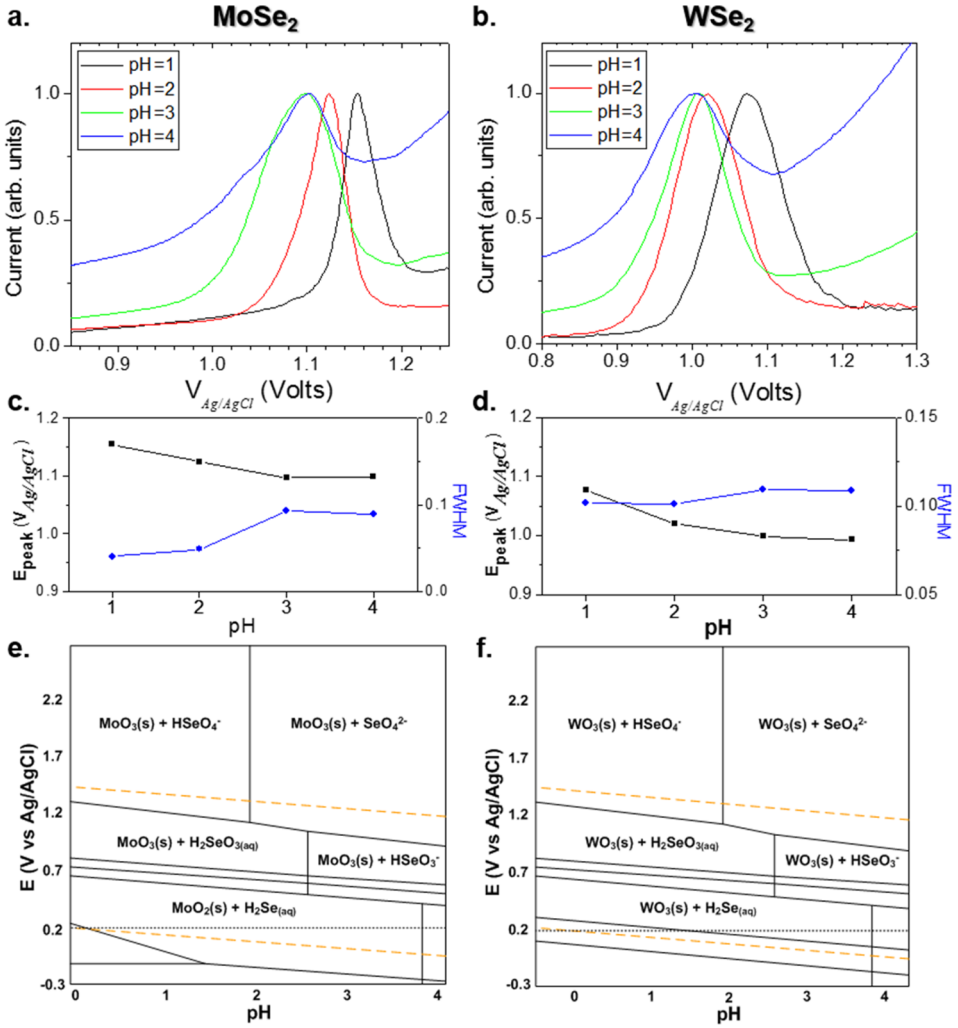

Figure 4. pH dependence of the EA process for transition metal diselenides. Voltammograms of mechanically exfoliated (a) $MoSe_2$ and (b) WSe_2 flakes on TiN in 1 M LiCl at different acidic solutions of pH = 1−4. The potential was swept from 0 to 2 V vs Ag/AgCl at a rate of 10 mV/s. The current values have been normalized to account for variations in surface flake density. Peak potential and fwhm as a function of pH for (c) $MoSe_2$ and (d) WSe_2. Pourbaix diagrams at 25 °C, 1 bar for (e) Mo−Se−OH and (f) W−Se−OH systems, generated from The Materials Project database.[51] The potential, $E_{Ag/AgCl}$, is in reference to the Ag/AgCl reference electrode (+0.197 V versus the standard hydrogen electrode).

respectively, show the dissolution/corrosion of the multilayer $MoSe_2$ and WSe_2 flakes after 10 s at the indicated specific applied potentials. For the $MoSe_2$ flakes, no visible corrosion occurred at potentials below the peak potential (E_{peak}), and limited corrosion started from the outer edges of the flakes at the peak potential of 1.1 V. However, once the applied potential exceeded the peak potential, multilayer flakes were actively corroded away leaving behind monolayer remnants. For the WSe_2 flakes, no visible corrosion occurred even at the peak potential of 1.0 V. However, beyond the peak anodic potential, complete corrosion took place from the WSe_2 flake perimeters without leaving behind any monolayer remnants. For both of these materials it was found that the electroablation process required overpotentials to corrode the multilayers. Also, the corrosion process occurred from the edges to the center of both bulk materials which is similar to our earlier findings on MoS_2 and WS_2. However, while the EA process on $MoSe_2$ yielded the monolayer, it was unsuccessful for obtaining the WSe_2 monolayer. As we will elucidate in the following sections through more detailed experiments and possible reaction pathways, the monolayer survival is strongly dependent on competing reaction rates between the monolayer and the bulk layers which in turn are determined by how the transition metal is bound to the chalcogen. As such, the electrochemical properties change as a consequence of altering the transition metal (Mo and W) or the chalcogen component (S and Se).[45]

The voltammetry plots for different pH values are shown in Figure 4a,b for $MoSe_2$ and WSe_2, respectively. For both $MoSe_2$ and WSe_2, the peak potential (E_{peak}) decreases with increasing pH between acidities of 1 to 4, which can be explained on the basis of the Nernst equation.[46] E_{peak} versus pH for $MoSe_2$ and WSe_2 is shown in Figure 4c,d, respectively. The slope of the E_{peak} versus pH curve for $MoSe_2$ was found to be ∼30 mV/pH, between pH = 1 and 2, which indicates a one-proton−two-electron transfer mechanism corresponding to oxidation of Mo-based dichalcogenides from Mo^{4+} to Mo^{6+} consistent with previous reports.[47,48] It is noted that the redox potential of a reaction involving m protons and n electrons shifts $(m/n) \times 59$ mV per 10-fold change in proton activity (which, in the case of water, is per pH unit). The larger slope of the E_{peak} versus pH curve for WSe_2 (∼55 mV/pH) suggests a different reaction mechanism (possibly one-proton−one-electron transfer mechanism) and hence can be related to the dissolution of

DOI: 10.1021/acsami.7b13107
ACS Appl. Mater. Interfaces 2017, 9, 39059−39068

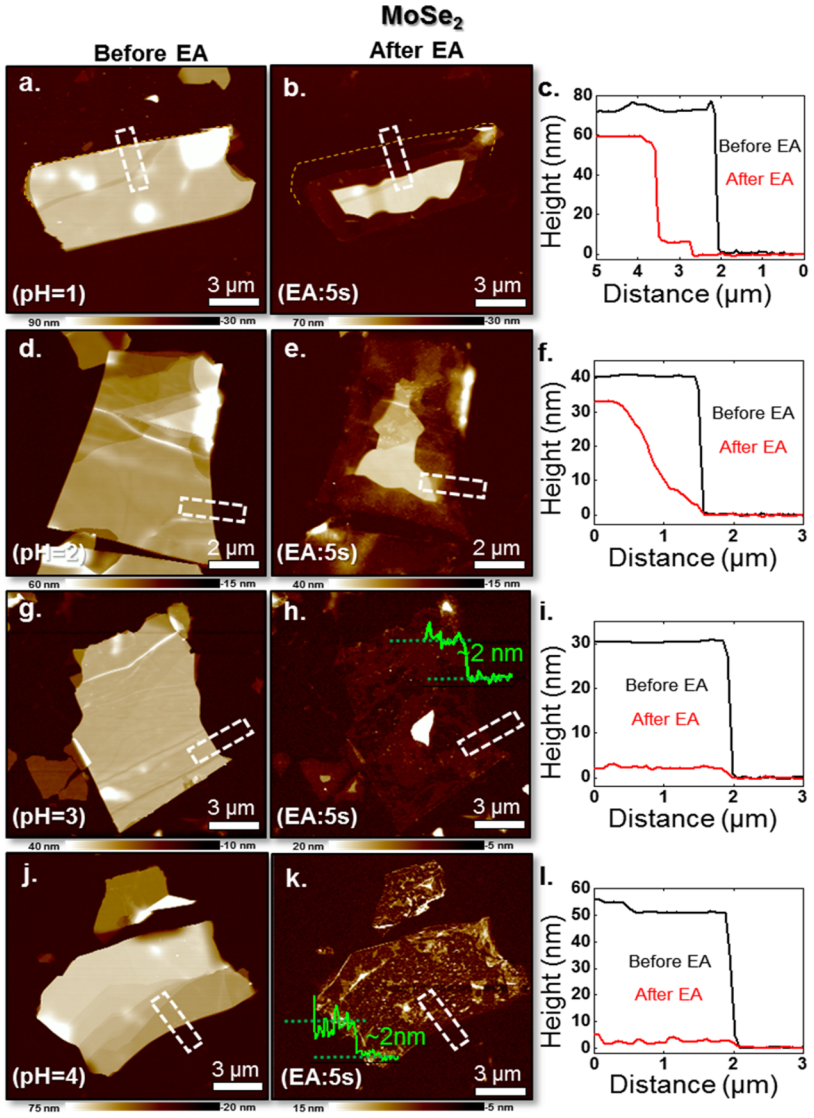

Figure 5. AFM images and height profiles for multilayer $MoSe_2$ flakes before and after 5 s of EA process in (a–c) pH = 1, (d–f) pH = 2, (g–i) pH = 3, and (j–l) pH = 4 solution.

monolayer WSe_2 unlike the survival of monolayer $MoSe_2$, under similar reaction conditions.[45] It is also noticeable that the peak shape varies from sharp (at pH 1) to broader (at pH 4) with increasing pH value for both $MoSe_2$ and WSe_2. When the value of the fwhm is larger, it is easier to activate the ions in the electrochemical reaction.[49,50] The peak broadening at higher pH values, therefore, suggests that more reactive species are involved in the corrosion process for $MoSe_2$ and WSe_2.

The oxidative dissolution kinetics of $MoSe_2$ and WSe_2 are complicated and involve the electro-activities of their edge planes, the formation of oxides, and their solubility. We propose two types of oxidative species that participate in and/or catalyze the corrosion of multilayer $MoSe_2$ and WSe_2: (1) the hydroxide ions (OH^-) which are present in the electrolyte solution and (2) oxidizing agents such as O_2, H_2O_2, etc., which are generated at the interface of TiN and the electrolyte as a result of the applied high anodic potentials.[52] These oxidizing agents gradually passivate the TiN substrate through the formation of TiO_2 following the reaction given by eq 1.[53] However, the passivation of TiN does not obscure the corrosion of $MoSe_2$ and WSe_2 since the passivation kinetics is significantly slower than the EA process.

$$TiN + 2H_2O \rightarrow TiO_2 + 1/2N_2 + 4H^+ + 4e^- \quad (1)$$

To explain the corrosion dynamics of $MoSe_2$, we postulate that oxygen, initially, gets chemisorbed at the edge planes of $MoSe_2$ to form O–Se bonds. DFT calculations show that the formation energy of oxygen adsorption from the O–Se bond (−0.284 eV) has a relatively lower stability compared to the energy of oxygen replacement Mo–O bond (−2.504 eV).[54,55] As such, the chemisorption is followed by desorption of oxygen with a possible "kick-out" of O–Se species. This leaves behind unsaturated bonds for the transition metal, which then is readily available to form Mo–O bonds in the presence of oxygen. Moreover, Se vacancies present at the edge planes further facilitate Mo–O bond formation. From viewing the Mo–O–Se Pourbaix diagram in Figure 4e, it is apparent that the most likely reaction products at different pH and potential ranges are MoO_3, $HSeO_4^-$, or SeO_4^{2-} as given by eq 2.[56,57] As for WSe_2, the O–Se (−0.132 eV) bond is even more unstable compared to the replacement of W–O bonds (−2.184 eV). For WSe_2, the

DOI: 10.1021/acsami.7b13107
ACS Appl. Mater. Interfaces 2017, 9, 39059–39068

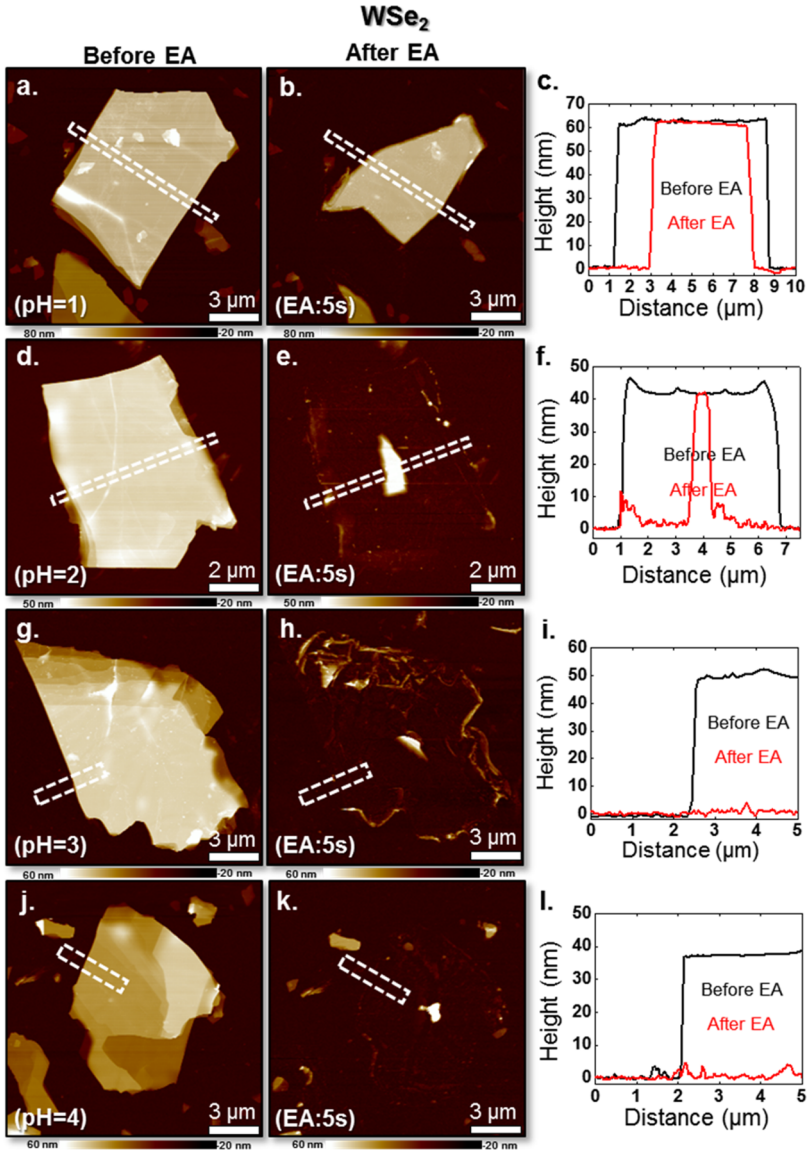

Figure 6. AFM images and height profiles for multilayer WSe_2 flakes before and after 5 s of EA process in (a–c) pH = 1, (d–f) pH = 2, (g–i) pH = 3, and (j–l) pH = 4 solution.

Pourbaix diagram in Figure 4f shows that the probable products are WO_3, $HSeO_4^-$, and SeO_4^{2-}.

$$MoSe_2\ (\text{or}\ WSe_2) + H_2O/O_2 \rightarrow MoO_3\ (\text{or}\ WO_3) + HSeO_4^-\ \text{or}\ SeO_4^{2-} \quad (2)$$

MoO_3 and WO_3 are known to be thermodynamically unstable and readily hydrolyzed into molybdate and tungstate following eq 3, which results in the dissolution of the oxide and hence completion of the corrosion process for the bulk layers.[58,59]

$$MoO_3\ (\text{or}\ WO_3) + 2OH^- \leftrightarrow MoO_4^{2-}\ (\text{or}\ WO_4^{2-}) + H_2O \quad (3)$$

Other studies also show that elemental species such as MoO_4^{2-} and SeO_4^{2-} could be generated at anodic potentials above 1.0 V.[60]

To explain the survival or dissolution of the monolayer after the EA treatment, we invoke a hypothesis which assumes a competing rate of corrosion for the layer in contact with the TiN substrate and the rest of the bulk layers. If the corrosion rate for the monolayer is much slower compared to the corrosion rate for the rest of the bulk layers, the monolayer will survive, as in the case of $MoSe_2$. However, if the corrosion rates are similar, the entire flake will dissolve without a monolayer remnant, as in the case of WSe_2. This suggests that, for $MoSe_2$, the covalent-type interaction between the monolayer edges and the TiN substrate is much stronger than that in the case of WSe_2. It is noted that this finding for the transition metal selenides is significantly different from that for the transition metal sulfides, where both MoS_2 and WS_2 monolayers survived after the EA treatment indicating much stronger monolayer/substrate interaction for the sulfides.

The mechanism of the oxidative dissolution for $MoSe_2$ was also studied by altering the OH^- concentration from 10^{-13} (pH = 1) to 10^{-10} (pH = 4) on a flake with similar lateral dimensions and thicknesses. Figure 5 shows the AFM height profiles for multilayer $MoSe_2$ flakes before and after 5 s of EA for different pH values. The EA process was conducted under a constant overpotential of 1.2 V for $MoSe_2$ and 1.1 V for WSe_2. It was found that the pH value plays an important role in the

DOI: 10.1021/acsami.7b13107
ACS Appl. Mater. Interfaces 2017, 9, 39059–39068

survival of monolayer $MoSe_2$ and also in the corrosion profile. For pH = 1, as shown in Figure 5a–c, the entire flake is slowly corroded from the edges into a smaller island without leaving any monolayer remnant. For pH = 2, as shown in Figure 5d–f, the flake is corroded from the edges into a pyramidal structure with some monolayer remnant. For pH = 3, as shown in Figure 5g–i, the flake is uniformly corroded from the edges into a much smaller island leaving a clean monolayer remnant. Finally, for pH = 4, as shown in Figure 5j–l, the flake is completely corroded away leaving a monolayer remnant. However, in the last instance, the monolayer remnant shows some nonuniformity. The pH-dependent monolayer survival can be explained with the help of differing corrosion rates for the bulk layers compared to that for the monolayer. It is reasonable to assume that the bulk layers have a much higher corrosion rate constant (k_B) owing to a weak van der Waals (VdW) interlayer interaction, whereas the corrosion rate constant for the monolayers (k_M's) are much smaller because of their strong covalent interaction with the substrate, i.e., $k_M \ll k_B$. However, the ultimate corrosion rate is determined not only by the corrosion rate constants but also by the available concentration of the oxidizing species ($[C_{OX}]$) that creates the Mo or W oxides and the hydroxide ions ($[OH^-]$) that are necessary for the dissolution of such oxides in the solution to complete the corrosion process. The reaction rate can be written as $r_{B,M} = k_{B,M}[C_{OX}][OH^-]$. At pH = 1, the concentration, $[C_{OX}]$, is likely to be limited by both a higher interfacial potential barrier at the electrolyte/electrode interface (i.e., smaller value for fwhm as discussed in the context of peak broadening in the voltammetry measurements in Figure 4a,b for the generation of oxidizing species) as well as diffusion of those species across the bulk layers. As such, the corrosion rate for the bulk layers (r_B) is comparable with the corrosion rate for the monolayers (r_M), i.e., $r_B \approx r_M$, and both have a low magnitude resulting in slow corrosion of the entire flake without any monolayer remnant. At pH = 2, the concentration, $[C_{OX}]$, increases slightly because of the lowering of the interfacial potential barrier at the electrolyte/electrode interface (i.e., larger value for fwhm); however, the $[OH^-]$ concentration is increased by an order of magnitude enhancing the bulk corrosion rate. The pyramidal shape of the corrosion profile can be explained from the Boltzmann–Poisson distribution of the OH^- ions across the bulk layers of the flake since the OH^- ions need to diffuse from the bulk solution toward the interface against the drift field that is present due to the positive potential applied to the TiN substrate. This would result in higher $[OH^-]$ concentration and hence a higher corrosion rate at the top of the flake which is furthest from the TiN interface. However, the bulk corrosion rate close to the interface can still be diffusion-limited which explains sporadic monolayer survival at pH = 2. At pH = 3, the $[OH^-]$ concentration becomes so large throughout the entire thickness of the flake that $r_B \gg r_M$. As such, the entire flake is rapidly corroded away to a tinier island leaving behind a clean monolayer remnant. For pH = 4 and above, the $[OH^-]$ concentration becomes extremely large such that even the monolayer corrosion becomes significant resulting in corrosion of the monolayer. Figure 6 shows the AFM height profiles for multilayer WSe_2 flakes before and after 5 s of EA for pH = 1, 2, 3, and 4. Unlike $MoSe_2$, there were no monolayer remnants for WSe_2 at any given pH value, indicating a much higher corrosion rate for WSe_2 monolayers. However, similar to $MoSe_2$, the bulk corrosion rate for WSe_2 was found to be much faster at higher pH.

CONCLUSION

The dynamics of the anomalous corrosion process, referred to as electroablation (EA), was investigated, and experimental outcomes were explained from a fundamental physical chemistry framework for the transition metal diselenides. We can engineer the EA process conditions and obtain monolayers of $MoSe_2$. However, the attempts to obtain monolayers of WSe_2 were unsuccessful because of its significantly higher corrosion rate. We proposed that the bulk layers have a much higher reaction rate constant owing to a weak van der Waals (VdW) interlayer interaction compared to that of their monolayer counterparts since the monolayers benefit from strong covalent interaction with the substrate. The rate constants also depend on the bond strength of the transition metal and the chalcogen atoms. As such, the corrosion properties differ when either the transition metal (Mo and W) or the chalcogen component (S and Se) is altered. The monolayer survival is, ultimately, determined by the competing corrosion dynamics between the bulk and the monolayer.

AUTHOR INFORMATION

Corresponding Author

*E-mail: sud70@psu.edu, das.sapt@gmail.com.

ORCID

Daniel S. Schulman: 0000-0002-0751-0578

Shien-Ping Feng: 0000-0002-3941-1363

Saptarshi Das: 0000-0002-0188-945X

Author Contributions

Y.T.H. and S.D. conceived the experiments and analyzed the data. Y.T.H., A.D., A.S., and D.B. performed all the experiments related to electrochemistry and did the monolayer characterization. D.S.S. assisted the experiments and analysis of materials. F.Z. performed the TEM experiments. The manuscript was written through contributions of all authors. All authors have given approval to the final version of the manuscript.

Notes

The authors declare no competing financial interest.

ACKNOWLEDGMENTS

The work of A.D., A.S., D.S.S., and S.D. was partially supported through Grant ECCS-1640020 from National Science Foundation (NSF) and Contract 2016-NE-2699 from Semiconductor Research Corporation. The work of Y.T.H. was supported by HKU exchange program, pilot scheme, and the General Research Fund from the Research Grants Council of Hong Kong Special Administrative Region, China, under Award 17202314 and 17204516 (S.-P.F.). The authors would also like to acknowledge useful discussion and critical insight from Dr. Mark W Horn.

REFERENCES

(1) Das, S.; Robinson, J. A.; Dubey, M.; Terrones, H.; Terrones, M. Beyond Graphene: Progress in Novel Two-Dimensional Materials and van der Waals Solids. *Annu. Rev. Mater. Res.* **2015**, *45*, 1–27.

(2) Das, S.; Chen, H.-Y.; Penumatcha, A. V.; Appenzeller, J. High Performance Multilayer MoS_2 Transistors with Scandium Contacts. *Nano Lett.* **2013**, *13*, 100–105.

(3) Das, S.; Appenzeller, J. WSe_2 Field Effect Transistors with Enhanced Ambipolar Characteristics. *Appl. Phys. Lett.* **2013**, *103*, 103501.

DOI: 10.1021/acsami.7b13107
ACS Appl. Mater. Interfaces 2017, 9, 39059–39068

(4) Das, S.; Gulotty, R.; Sumant, A. V.; Roelofs, A. All Two-Dimensional, Flexible, Transparent, and Thinnest Thin Film Transistor. *Nano Lett.* **2014**, *14*, 2861−2866.
(5) Krasnozhon, D.; Lembke, D.; Nyffeler, C.; Leblebici, Y.; Kis, A. MoS_2 Transistors Operating at Gigahertz Frequencies. *Nano Lett.* **2014**, *14*, 5905−5911.
(6) Sanne, A.; Ghosh, R.; Rai, A.; Yogeesh, M. N.; Shin, S. H.; Sharma, A.; Jarvis, K.; Mathew, L.; Rao, R.; Akinwande, D.; Banerjee, S. Radio Frequency Transistors and Circuits Based on Cvd MoS_2. *Nano Lett.* **2015**, *15*, 5039−5045.
(7) Das, S. Two Dimensional Electrostrictive Field Effect Transistor (2d-Efet): A Sub-60mv/Decade Steep Slope Device with High on Current. *Sci. Rep.* **2016**, *6*, 34811.
(8) Arnold, A. J.; Razavieh, A.; Nasr, J. R.; Schulman, D. S.; Eichfeld, C. M.; Das, S. Mimicking Neurotransmitter Release in Chemical Synapses Via Hysteresis Engineering in MoS_2 Transistors. *ACS Nano* **2017**, *11*, 3110−3118.
(9) Lee, H. S.; Min, S. W.; Park, M. K.; Lee, Y. T.; Jeon, P. J.; Kim, J. H.; Ryu, S.; Im, S. MoS_2 Nanosheets for Top−Gate Nonvolatile Memory Transistor Channel. *Small* **2012**, *8*, 3111−3115.
(10) Sahoo, R.; Pal, A.; Pal, T. 2D Materials for Renewable Energy Storage Devices: Outlook and Challenges. *Chem. Commun.* **2016**, *52*, 13528−13542.
(11) Wang, L.; Wang, Y.; Wong, J. I.; Palacios, T.; Kong, J.; Yang, H. Y. Functionalized MoS_2 Nanosheet-Based Field-Effect Biosensor for Label-Free Sensitive Detection of Cancer Marker Proteins in Solution. *Small* **2014**, *10*, 1101−1105.
(12) Yu, C. H.; Fan, M. L.; Yu, K. C.; Hu, V. P. H.; Su, P.; Chuang, C. T. Evaluation of Monolayer and Bilayer 2-D Transition Metal Dichalcogenide Devices for Sram Applications. *IEEE Trans. Electron Devices* **2016**, *63*, 625−630.
(13) Lee, L. T. L.; He, J.; Wang, B.; Ma, Y.; Wong, K. Y.; Li, Q.; Xiao, X.; Chen, T. Few-Layer $MoSe_2$ Possessing High Catalytic Activity Towards Iodide/Tri-Iodide Redox Shuttles. *Sci. Rep.* **2015**, *4*, 4063.
(14) Huang, Y.-J.; Fan, M.-S.; Li, C.-T.; Lee, C.-P.; Chen, T.-Y.; Vittal, R.; Ho, K.-C. $MoSe_2$ Nanosheet/Poly(3,4-Ethylenedioxythiophene): Poly(Styrenesulfonate) Composite Film as a Pt-Free Counter Electrode for Dye-Sensitized Solar Cells. *Electrochim. Acta* **2016**, *211*, 794−803.
(15) Koppens, F. H. L.; Mueller, T.; Avouris, P.; Ferrari, A. C.; Vitiello, M. S.; Polini, M. Photodetectors Based on Graphene, Other Two-Dimensional Materials and Hybrid Systems. *Nat. Nanotechnol.* **2014**, *9*, 780−793.
(16) Mao, J.; Yu, Y.; Wang, L.; Zhang, X.; Wang, Y.; Shao, Z.; Jie, J. Ultrafast, Broadband Photodetector Based on $MoSe_2$/Silicon Heterojunction with Vertically Standing Layered Structure Using Graphene as Transparent Electrode. *Adv. Sci.* **2016**, *3*, 1600018.
(17) Palacios-Berraquero, C.; Barbone, M.; Kara, D. M.; Chen, X.; Goykhman, I.; Yoon, D.; Ott, A. K.; Beitner, J.; Watanabe, K.; Taniguchi, T.; Ferrari, A. C.; Atatüre, M. Atomically Thin Quantum Light-Emitting Diodes. *Nat. Commun.* **2016**, *7*, 12978.
(18) Clark, G.; Schaibley, J. R.; Ross, J.; Taniguchi, T.; Watanabe, K.; Hendrickson, J. R.; Mou, S.; Yao, W.; Xu, X. Single Defect Light-Emitting Diode in a Van Der Waals Heterostructure. *Nano Lett.* **2016**, *16*, 3944−3948.
(19) Yin, Z.; Zhang, X.; Cai, Y.; Chen, J.; Wong, J. I.; Tay, Y.-Y.; Chai, J.; Wu, J.; Zeng, Z.; Zheng, B.; Yang, H. Y.; Zhang, H. Preparation of MoS_2−MoS_3 Hybrid Nanomaterials for Light-Emitting Diodes. *Angew. Chem., Int. Ed.* **2014**, *53*, 12560−12565.
(20) Yang, W.; Shang, J.; Wang, J.; Shen, X.; Cao, B.; Peimyoo, N.; Zou, C.; Chen, Y.; Wang, Y.; Cong, C.; Huang, W.; Yu, T. Electrically Tunable Valley-Light Emitting Diode (Vled) Based on Cvd-Grown Monolayer WS_2. *Nano Lett.* **2016**, *16*, 1560−1567.
(21) Salehzadeh, O.; Djavid, M.; Tran, N. H.; Shih, I.; Mi, Z. Optically Pumped Two-Dimensional MoS_2 Lasers Operating at Room-Temperature. *Nano Lett.* **2015**, *15*, 5302−5306.
(22) Pospischil, A.; Mueller, T. Optoelectronic Devices Based on Atomically Thin Transition Metal Dichalcogenides. *Appl. Sci.* **2016**, *6*, 78.
(23) Li, H.; Lu, G.; Wang, Y.; Yin, Z.; Cong, C.; He, Q.; Wang, L.; Ding, F.; Yu, T.; Zhang, H. Mechanical Exfoliation and Characterization of Single- and Few-Layer Nanosheets of WSe_2, TaS_2, and $TaSe_2$. *Small* **2013**, *9*, 1974−1981.
(24) Huang, Y.-K.; Cain, J. D.; Peng, L.; Hao, S.; Chasapis, T.; Kanatzidis, M. G.; Wolverton, C.; Grayson, M.; Dravid, V. P. Evaporative Thinning: A Facile Synthesis Method for High Quality Ultrathin Layers of 2d Crystals. *ACS Nano* **2014**, *8*, 10851−10857.
(25) Lee, G.; Lee, J.-Y.; Lee, G.-H.; Kim, J. Tuning the Thickness of Black Phosphorus Via Ion Bombardment-Free Plasma Etching for Device Performance Improvement. *J. Mater. Chem. C* **2016**, *4*, 6234−6239.
(26) Wang, D.; Wang, Y.; Chen, X.; Zhu, Y.; Zhan, K.; Cheng, H.; Wang, X. Layer-by-Layer Thinning of Two-Dimensional MoS_2 Films by Using a Focused Ion Beam. *Nanoscale* **2016**, *8*, 4107−4112.
(27) Wang, X.; Gong, Y.; Shi, G.; Chow, W. L.; Keyshar, K.; Ye, G.; Vajtai, R.; Lou, J.; Liu, Z.; Ringe, E.; Tay, B. K.; Ajayan, P. M. Chemical Vapor Deposition Growth of Crystalline Monolayer $MoSe_2$. *ACS Nano* **2014**, *8*, 5125−5131.
(28) Lee, Y.-H.; Zhang, X.-Q.; Zhang, W.; Chang, M.-T.; Lin, C.-T.; Chang, K.-D.; Yu, Y.-C.; Wang, J. T.-W.; Chang, C.-S.; Li, L.-J.; Lin, T.-W. Synthesis of Large-Area MoS_2 Atomic Layers with Chemical Vapor Deposition. *Adv. Mater.* **2012**, *24*, 2320−2325.
(29) Dumcenco, D.; Ovchinnikov, D.; Marinov, K.; Lazić, P.; Gibertini, M.; Marzari, N.; Sanchez, O. L.; Kung, Y.-C.; Krasnozhon, D.; Chen, M.-W.; Bertolazzi, S.; Gillet, P.; Fontcuberta i Morral, A.; Radenovic, A.; Kis, A. Large-Area Epitaxial Monolayer MoS_2. *ACS Nano* **2015**, *9*, 4611−4620.
(30) Kim, H.; Ovchinnikov, D.; Deiana, D.; Unuchek, D.; Kis, A. Suppressing Nucleation in Metal−Organic Chemical Vapor Deposition of MoS_2 Monolayers by Alkali Metal Halides. *Nano Lett.* **2017**, *17*, 5056−5063.
(31) Das, S.; Bera, M. K.; Tong, S.; Narayanan, B.; Kamath, G.; Mane, A.; Paulikas, A. P.; Antonio, M. R.; Sankaranarayanan, S. K.; Roelofs, A. K. A Self-Limiting Electro-Ablation Technique for the Top-Down Synthesis of Large-Area Monolayer Flakes of 2d Materials. *Sci. Rep.* **2016**, *6*, 28195.
(32) Voiry, D.; Yamaguchi, H.; Li, J.; Silva, R.; Alves, D. C.; Fujita, T.; Chen, M.; Asefa, T.; Shenoy, V. B.; Eda, G.; Chhowalla, M. Enhanced Catalytic Activity in Strained Chemically Exfoliated WS_2 Nanosheets for Hydrogen Evolution. *Nat. Mater.* **2013**, *12*, 850−855.
(33) Lin, S. H.; Kuo, J. L. Activating and Tuning Basal Planes of MoO_2, MoS_2, and $MoSe_2$ for Hydrogen Evolution Reaction. *Phys. Chem. Chem. Phys.* **2015**, *17*, 29305−29310.
(34) Larentis, S.; Fallahazad, B.; Tutuc, E. Field-Effect Transistors and Intrinsic Mobility in Ultra-Thin $MoSe_2$ Layers. *Appl. Phys. Lett.* **2012**, *101*, 223104.
(35) Morales, J.; Santos, J.; Tirado, J. L. Electrochemical Studies of Lithium and Sodium Intercalation in $MoSe_2$. *Solid State Ionics* **1996**, *83*, 57−64.
(36) Lundt, N.; Maryński, A.; Cherotchenko, E.; Pant, A.; Fan, X.; Tongay, S.; Sęk, G.; Kavokin, A. V.; Höfling, S.; Schneider, C. Monolayered $MoSe_2$: A Candidate for Room Temperature Polaritonics. *2D Mater.* **2017**, *4*, 015006.
(37) Chen, Z.; Liu, H.; Chen, X.; Chu, G.; Chu, S.; Zhang, H. Wafer-Size and Single-Crystal $MoSe_2$ Atomically Thin Films Grown on Gan Substrate for Light Emission and Harvesting. *ACS Appl. Mater. Interfaces* **2016**, *8*, 20267−20273.
(38) Das, S.; Prakash, A.; Salazar, R.; Appenzeller, J. Toward Low-Power Electronics: Tunneling Phenomena in Transition Metal Dichalcogenides. *ACS Nano* **2014**, *8*, 1681−1689.
(39) Bradley, A. J.; Ugeda, M. M.; da Jornada, F. H.; Qiu, D. Y.; Ruan, W.; Zhang, Y.; Wickenburg, S.; Riss, A.; Lu, J.; Mo, S. K.; Hussain, Z.; Shen, Z. X.; Louie, S. G.; Crommie, M. F. Probing the Role of Interlayer Coupling and Coulomb Interactions on Electronic Structure in Few-Layer $MoSe_2$ Nanostructures. *Nano Lett.* **2015**, *15*, 2594−2599.
(40) Tonndorf, P.; Schmidt, R.; Böttger, P.; Zhang, X.; Börner, J.; Liebig, A.; Albrecht, M.; Kloc, C.; Gordan, O.; Zahn, D. R. T.;

DOI: 10.1021/acsami.7b13107
ACS Appl. Mater. Interfaces 2017, 9, 39059−39068

Michaelis de Vasconcellos, S.; Bratschitsch, R. Photoluminescence Emission and Raman Response of Monolayer MoS_2, $MoSe_2$, and WSe_2. *Opt. Express* **2013**, *21*, 4908−4916.
(41) Li, H.; Tsai, C.; Koh, A. L.; Cai, L.; Contryman, A. W.; Fragapane, A. H.; Zhao, J.; Han, H. S.; Manoharan, H. C.; Abild-Pedersen, F.; Nrskov, J. K.; Zheng, X. Activating and Optimizing MoS_2 Basal Planes for Hydrogen Evolution through the Formation of Strained Sulphur Vacancies. *Nat. Mater.* **2015**, *15*, 48−53.
(42) Nam, D.; Lee, J.-U.; Cheong, H. Excitation Energy Dependent Raman Spectrum of $MoSe_2$. *Sci. Rep.* **2015**, *5*, 17113.
(43) Soubelet, P.; Bruchhausen, A. E.; Fainstein, A.; Nogajewski, K.; Faugeras, C. Resonance Effects in the Raman Scattering of Monolayer and Few-Layer $MoSe_2$. *Phys. Rev. B: Condens. Matter Mater. Phys.* **2016**, *93*, 155407.
(44) Nam, D.; Lee, J.-U.; Cheong, H. Excitation Energy Dependent Raman Spectrum of $MoSe_2$. *Sci. Rep.* **2015**, *5*, 17113.
(45) Eng, A. Y. S.; Ambrosi, A.; Sofer, Z.; Šimek, P.; Pumera, M. Electrochemistry of Transition Metal Dichalcogenides: Strong Dependence on the Metal-to-Chalcogen Composition and Exfoliation Method. *ACS Nano* **2014**, *8*, 12185−12198.
(46) Walczak, M. M.; Dryer, D. A.; Jacobson, D. D.; Foss, M. G.; Flynn, N. T. Ph Dependent Redox Couple: An Illustration of the Nernst Equation. *J. Chem. Educ.* **1997**, *74*, 1195−1197.
(47) Zafir Mohamad Nasir, M.; Sofer, Z.; Pumera, M. Effect of Electrolyte pH on the Inherent Electrochemistry of Layered Transition-Metal Dichalcogenides (MoS_2, $MoSe_2$, WS_2, WSe_2). *ChemElectroChem* **2015**, *2*, 1713−1718.
(48) Mayer, J. M. Proton-Coupled Electron Transfer: A Reaction Chemist's View. *Annu. Rev. Phys. Chem.* **2004**, *55*, 363−390.
(49) Guidelli, R.; Compton, R. G.; Feliu, J. M.; Gileadi, E.; Lipkowski, J.; Schmickler, W.; Trasatti, S. Defining the Transfer Coefficient in Electrochemistry: An Assessment (Iupac Technical Report). *Pure Appl. Chem.* **2014**, *86*, 245−258.
(50) Brownson, D. A. C.; Banks, C. E. *The Handbook of Graphene Electrochemistry*, 1st ed.; Springer-Verlag: London, 2014.
(51) Jain, A.; Ong, S. P.; Hautier, G.; Chen, W.; Richards, W. D.; Dacek, S.; Cholia, S.; Gunter, D.; Skinner, D.; Ceder, G.; Persson, K. A. The Materials Project: A materials genome approach to accelerating materials innovation. *APL Mater.* **2013**, *1*, 011002.
(52) Wang, Z.; von dem Bussche, A.; Qiu, Y.; Valentin, T. M.; Gion, K.; Kane, A. B.; Hurt, R. H. Chemical Dissolution Pathways of MoS_2 Nanosheets in Biological and Environmental Media. *Environ. Sci. Technol.* **2016**, *50*, 7208−7217.
(53) Avasarala, B.; Haldar, P. Electrochemical Oxidation Behavior of Titanium Nitride Based Electrocatalysts under Pem Fuel Cell Conditions. *Electrochim. Acta* **2010**, *55*, 9024−9034.
(54) Azcatl, A.; KC, S.; Peng, X.; Lu, N.; McDonnell, S.; Qin, X.; de Dios, F.; Addou, R.; Kim, J.; Kim, M. J.; Cho, K.; Wallace, R. M. HfO_2 on Uv−O_3 Exposed Transition Metal Dichalcogenides: Interfacial Reactions Study. *2D Mater.* **2015**, *2*, 014004.
(55) Liu, H.; Han, N.; Zhao, J. Atomistic Insight into the Oxidation of Monolayer Transition Metal Dichalcogenides: From Structures to Electronic Properties. *RSC Adv.* **2015**, *5*, 17572−17581.
(56) Ohmori, T.; Castro, R. J.; Cabrera, C. R. Surface Modification of $MoSe_2$ in Solution Using a Combined Technique of Scanning Tunneling Microscopy Indentation with Electrochemical Etching. *Langmuir* **1998**, *14*, 6287−6290.
(57) Saji, V. S.; Lee, C.-W. Selenium Electrochemistry. *RSC Adv.* **2013**, *3*, 10058−10077.
(58) Chia, X.; Eng, A. Y. S.; Ambrosi, A.; Tan, S. M.; Pumera, M. Electrochemistry of Nanostructured Layered Transition-Metal Dichalcogenides. *Chem. Rev.* **2015**, *115*, 11941−11966.
(59) Wang, Z.; Zhu, W.; Qiu, Y.; Yi, X.; von dem Bussche, A.; Kane, A.; Gao, H.; Koski, K.; Hurt, R. Biological and Environmental Interactions of Emerging Two-Dimensional Nanomaterials. *Chem. Soc. Rev.* **2016**, *45*, 1750−1780.
(60) Chia, X.; Ambrosi, A.; Sofer, Z.; Luxa, J.; Pumera, M. Catalytic and Charge Transfer Properties of Transition Metal Dichalcogenides Arising from Electrochemical Pretreatment. *ACS Nano* **2015**, *9*, 5164−5179.

NOTE ADDED AFTER ASAP PUBLICATION

This paper published ASAP on 10/26/2017. The affiliations were modified and the corrected version was reposted on 10/27/2017.

DOI: 10.1021/acsami.7b13107
ACS Appl. Mater. Interfaces 2017, 9, 39059−39068